Progress Report 2010 and Beam Request for 2011

Muon Capture on the Deuteron

The MuSun Experiment

PSI Experiment R-08-01, spokespersons P. Kammel, C. Petitjean, A.A. Vasilyev

MuSun Collaboration [1]

Petersburg Nuclear Physics Institute – University of Washington Seattle – Paul Scherrer Institut – University of Kentucky – Boston University – Regis University – University of South Carolina– Université Catholique de Louvain

http://muon.npl.washington.edu/exp/MuSun

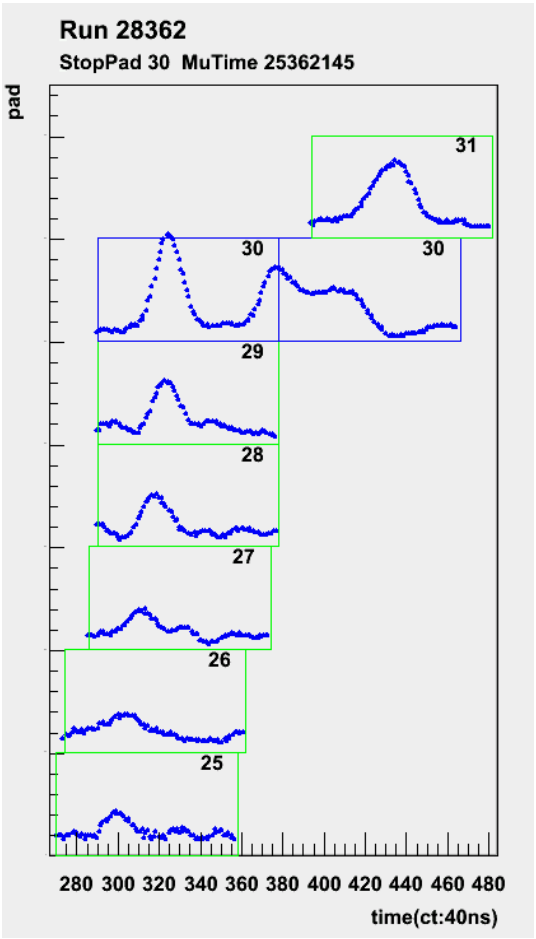

Figure 1: Event display from Run Fall 2010. A muon stops in the TPC, in the volume above pad 30. Subsequently the muon catalyzes a $dd \rightarrow p + t$ fusion, which is seen as delayed pulses on pad 30 and 31.

Contents

1 Overview

1.1 Physics Update and Experimental Strategy

The goal of the MuSun experiment is a measurement of the rate Λ_d for the semileptonic weak process

$$\mu^- + d \rightarrow \nu_\mu + n + n \tag{1}$$

to a precision of better than 1.5%. Λ_d denotes the capture rate from the doublet hyperfine state of the muonic deuterium atom in its $1s$ ground state.

Muon capture on the deuteron is the simplest weak interaction process on a nucleus and can both be calculated and measured to a high degree of precision — see the discussion in a recent review of this field [2]. The basic pseudoscalar coupling g_P required for such calculations has been measured by the MuCap experiment [3] and will be more precisely determined by its ongoing final analysis. At the same time, effective field theories (EFTs) have been developed to calculate electro-weak observables in few-body systems, following Weinberg's pioneering work [4]. The standard nuclear physics approach (SNPA), based on the impulse approximation with explicit modeling of two body current contributions, is being replaced by less model-dependent hybrid EFT [5] and pionless EFT [6] calculations, see Table 1. The prospect of a precise MuSun result has stimulated the recent calculations. Visits and presentations by some authors of these papers at PSI promoted efforts [7] to resolve the discrepancy between Ref. [8] and Refs. [5, 9]. Several theory groups [10] are preparing fully self-consistent calculations in a rigorous QCD-based EFT scheme.

Λ_q	Λ_d	year	Reference	method
	397-400	1990	[11]	SNPA
	416±7	1990	[12]	SNPA
	386	2001	[5]	EFT*
11.4	416±6	2009	[8]	SNPA, EFT*
	392.0±2.3	2010	[9]	EFT*

Table 1: Recent theoretical results of muon capture rates from the quartet (Λ_q) and doublet (Λ_d) state of the μd atom, respectively. EFT* denotes a hybrid EFT calculation. The recent pionless EFT calculation [13] cannot be expressed by a single value and therefore is not included in the table.

While reaction (1) could serve as the benchmark for the axial current interaction in the two-nucleon system, the present experimental situation is inadequate to provide much guidance. The best existing experiments [14, 15] are not precise enough and the most precise result differs from modern theory by 3 standard deviations. If true, such a discrepancy would have major ramifications for important astrophysics processes, which are discussed below. The MuSun measurement, based on novel techniques, should exceed the precision of previous efforts by nearly an order of magnitude.

Reaction (1) is closely related to fundamental reactions of astrophysical interest. These include the $p + p$ fusion reaction, which is the primary energy source in the sun and the main sequence stars, and the $\nu + d$ reaction, which provided convincing evidence for solar neutrino oscillations at the Sudbury Neutrino Observatory [16]. Direct experiments on the axial-vector interaction within the two-nucleon system are scarce and do not have nearly the required precision [17, 18]. Here again, the development of EFTs during the last years has led to an important model-independent connection. It was proved that, up to the required precision in the systematic chiral expansion, these weak reactions are related by a two-nucleon

current term, whose strength is parametrized by a single, but poorly known low-energy constant [19, 20]. For the foreseeable future, the MuSun experiment is the cleanest and only way to determine this constant to a precision 5 times greater than presently available.

The MuSun experiment must be performed under conditions such that the result leads to an unambiguous extraction of Λ_d, independent of muonic atomic physics complications. The transition between the upper μd quartet to the lower μd hyperfine state is slow and, once a $dd\mu$ molecule is formed, nuclear dd fusion occurs at a time scale of nanoseconds (because of the process of muon-catalyzed fusion). Our studies demonstrated that atomic physics uncertainties are reduced to a negligible level at optimized target conditions of T = 30 K and $\phi = 6\%$ liquid hydrogen density (ϕ refers to the deuterium density normalized to liquid hydrogen density). To achieve such conditions, a new high-density cryogenic ionization chamber filled with ultra-pure deuterium is being developed. This TPC will define the muon stop, identify impurities, and observe muon-catalyzed reactions. The new TPC must have very good energy resolution and full analog readout using flash ADCs. This information is critical to avoid systematic uncertainties in the muon stop definition and to detect the charged particles induced by the fusion and impurity capture processes. The 5-times higher target density of MuSun, compared to MuCap, implies that the chamber does not have internal gas gain and that drift voltages up to 100 kV are needed.

1.2 Milestones

- **PAC approval.** The MuSun experiment was approved by the PSI PAC in spring 2008.
- **First Test Run in 2008.** An existing MuCap TPC operating at room temperature was rebuilt with several newly-developed components as a test and proof of principle of the new detector technology.
- **Main External Funding Approved.** In fall 2008, several groups within the collaboration submitted requests to their funding agencies. The physics case was well received and funding was approved in spring 2009.
- **MuSun Collaboration Grows.** Since proposal submission, 5 Ph.D. students, 2 diploma students and 2 new postdocs have joined the experiment. Additionally, 3 undergraduates will join for the upcoming summer 2011 beam time.
- **Development of the Full CryoTPC Setup.** The construction and test of the CryoTPC and the associated cooling and vacuum components was led by the PNPI team.
- **Strong Endorsement of MuSun by BVR 41.** After consultation with experts in the field, the PAC further endorsed the theoretical motivation and importance of the MuSun experiment.
- **First Successful Run with CryoTPC in 2010.** In 2010 MuSun became operational. A short engineering run in spring 2010 (run **R2010a**) demonstrated successful operation of the MuSun detector with the TPC working stably under nominal cryo-conditions. After rectifying several shortcomings of this initial test - in particular noise, spark and grounding issues - the whole system was fully commissioned during 8 weeks of beam time in $\pi E3$ in fall 2010 (run **R2010b**), including several weeks of quality data taking.
- **Testbeam in $\pi E1$ 2010.** In fall 2010, the PSI team also conducted a one week long beam test in the area $\pi E1$. It led to promising results concerning the continuation of MuSun and, more generally, experiments requiring excellent μ^- beams in an expanded $\pi E1$ after 2011.

2 Run Overview

2.1 Run R2010a

In spring 2010, soon after the full assembly of the CryoTPC, the whole beam-line, detector and cryo-system was combined for the first time for a beam test in $\pi E3$. The cryo-performance of the system was excellent and high gas purity was obtained. However, the muon identification suffered from several problems. The main grid HV often broke down, smaller discharges led to large pick-up on the signal lines and the noise and RF-pickup overwhelmed muon signals. Setting the waveform digitizer (WFD) thresholds close to the noise proved difficult. As a result of these issues, only large fusion pulses could be detected on the TPC with high efficiency. The DAQ was modified to handle the high digitizer rates. The electron-wire chambers worked well, but some readouts showed repetitive oscillations, so that several detector sections were turned off to allow stable data taking. In the intervening months after the run, intense work continued on hardware and analysis software, to fix most problems before the fall R2010b run. Some details of these improvements are given in section 3.

2.2 Run R2010b

The first beam weeks in the fall of 2010 were used for set-up and further debugging of hardware problems. After that, quite stable data-taking conditions were achieved. Muon tracks and fusions were clearly identified, boosting also the development of the analysis software now being challenged with real data. The quality of this data is almost production level, with one deficiency being the insufficient isotopic purity of the deuterium used. The protium concentration was $c_p \approx 0.002$, which leads to a systematic correction of approximately 50 Hz (see Section 5.1). However, that does not prevent us from performing the planned systematic and consistency checks with a statistically significant data set.

The R2010b run produced a total of 13.6 terabytes (TB) of data. Roughly 10.6 TB passed an initial quality check, with 8.3 TB corresponding to μ^- events and 2.3 TB to μ^+. Scintillation counters placed just at the end of the beamline registered approximately 3.4×10^6 muons entering the TPC per data file (between 3 and 4 minutes of data taking). Of the muon entrances, a simple online analysis indicated that roughly 50% result in good muon stops in the TPC. Roughly 62% of these muon stops yield one or more decay electrons. Here an electron requires a fully reconstructed track in the electron chambers and a 4-fold coincidence in the gondola scintillator detectors. We estimate that R2010b will yield a total of 5×10^9 good μ^- stops with coincident decay electrons.

After sorting out some beamline magnet settings, successful ~40 MeV/c beam tunes were established for both beam polarities. The electrostatic kicker was run in muon–on–request mode, (allowing single muons for 25μs at a time by diverting the beam) achieving a muon extinction factor of 120 for μ^-.

The TPC was read out with waveform digitizers with a sampling rate of 25 MHz. The WFDs were operated mostly in a self-triggered mode, allowing clean collection of muon stop pulses without being swamped by noise. For diagnostic purposes, the entire TPC was occasionally read out by means of an external forced trigger. The muon detectors were aligned and calibrated and operated in a stable mode throughout the run. The electron wire chambers tended to lose many channels at the beginning of the run, but the operational condition improved significantly throughout the first few weeks. The electron scintillator detectors were calibrated and worked well throughout the run. In order to allow for a fully blind analysis of the lifetime, the clock frequency of all digitizers was slightly detuned and recorded by someone outside the collaboration.

The data acquisition system was robust throughout the run, with timely recovery following

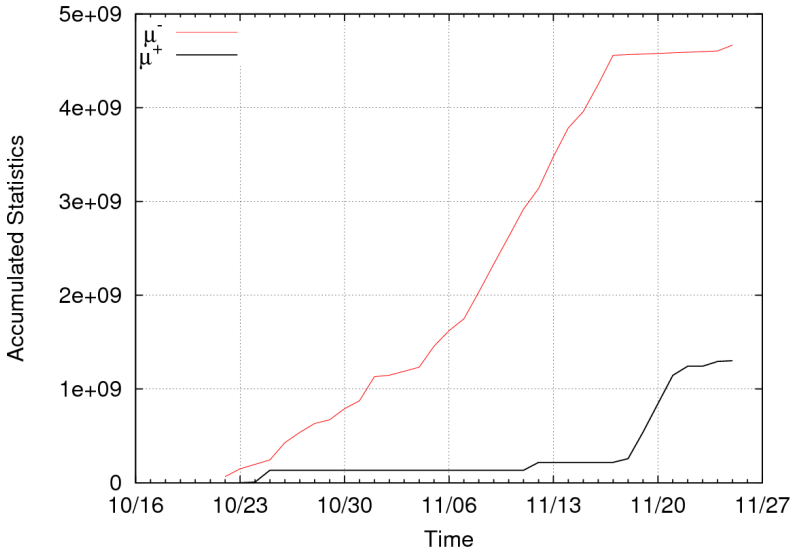

Figure 2: Accumulated statistics (muon and decay electron pairs) for μ^- (red) and μ^+ (black).

any critical failure. The live time was typically 75-80%. Data quality diagnostics included the slow control system for the CryoTPC, a low-statistics online analysis, and a higher-statistics offline analysis provided by a small local computing cluster.

3 System Status and Performance

3.1 DAQ

The data acquisition system (DAQ) in the MuSun experiment provides the readout of frontend electronics, event assembling, data logging, online data monitoring, hardware monitoring and control. It uses experience, DAQ software and hardware components from the MuCap and MuLan experiments. The MuSun DAQ consists of seven frontend computers, one backend computer, redundant array of independent disks (RAID) storage, a tape robot, three computers for hardware control and monitoring, and a mini-cluster of four computers for a fast offline data analysis (Fig. 3). The DAQ reads the data from frontend electronics in deadtime-free segments of variable length (MIDAS events). A segment can be terminated by "buffer almost full" signals from various hardware modules or a fixed timeout. The typical segment length during production data-taking is about 100 ms. Some frontend electronics modules continuously read out while the segment is active; others read out on segment completion. The time between segments determines the deadtime of the DAQ.

The main DAQ in MuSun is a Linux-based system integrated into the MIDAS framework. However, the control and monitoring of CHUPS and CryoTPC is separated into a completely independent system running under the Microsoft Windows operating system. The separation of a functionally independent CryoTPC DAQ into an autonomous system was important both for practical and safety reasons. The main DAQ periodically receives snapshots of TPC parameters using a TCP/IP network connection and writes them into the MIDAS data stream. The control of CryoTPC parameters is accomplished through a custom graphical user interface rather than through the MIDAS online database. The alarm system provides watchdogs on the most critical parameters in order to inform the operators about dangerous situations. The operation of CHUPS and CryoTPC systems was very stable during the run.

For the production running in 2010, the backend computer was replaced by a faster and more powerful new machine based on an Intel Xeon quad-core CPU. At the beginning of

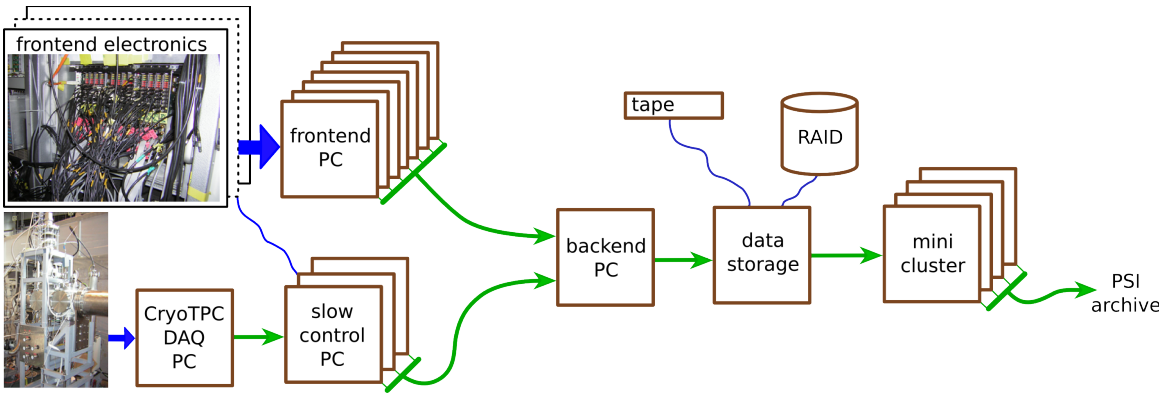

Figure 3: Block diagram of data acquisition system (DAQ).

the run the DAQ had stability problems due to its inability to handle large data rates from noisy hardware. During the production data-taking the DAQ ran smoothly without any serious interruptions. The livetime of the DAQ was about 80% at a typical data rate of ~ 8 MB/s. Two copies of the data were recorded during the run. A master copy was written to 400 MB LTO3 tapes for transportation to USA for offline analysis at the National Center for Supercomputing Applications (NCSA). A backup copy was stored in the PSI archive for independent offline analysis by the PNPI group.

The digitization and readout of pulses from TPC pads is performed with the BU 8-bit waveform digitizers (WFDs), taking into account the experience from the MuSun engineering run in 2009. The traditional MuCap system, based on custom built time-to-digital converters TDC400, was completely eliminated. The MuCap 12-bit flash analog-to-digital converters (FADCs) were exclusively used for the digitization and readout of pulses from neutron detectors.

Changes in the WFD firmware allowed us to operate the WFDs in a self-triggering mode with a digital threshold. The implementation of digital triggering was a significant improvement since the digital threshold was found to be much less sensitive to high-frequency noise. This allowed us to carefully adjust all thresholds on the TPC pads as low as possible above the noise and to avoid situations when occasional noise would result in a high stream of useless data.

Another significant addition to WFD firmware was the implementation of a digitization mode by an external trigger. Using a greatly prescaled muon arrival trigger, it was used to record waveforms on all 48 TPC pads for a 16 μs time interval. These data give a most complete picture of reaction kinematics in the active volume of the TPC and provide valuable information for developing and testing the algorithms for identification of clean muon stops.

3.2 Beam Detectors

The muon detectors in MuSun were inherited from the MuCap experiment without any major modifications. The most upstream muon detector is a 0.5 mm thick scintillator detector, the μSC, which provides a fast timing signal for the "start" of the lifetime measurement. It is followed by a second scintillator detector, the μSCA, with a 35-mm-diameter hole in the middle to allow beam particles to pass. Signals from the μSCA can be used to veto any off-axis muons. The third muon detector is a multi-wire proportional chamber, the μPC, which provides horizontal (X) and vertical (Y) positions of beam particles. The threshold in μPC was adjusted to trigger on beam muons and to be immune to most of the beam electrons. The typical X-Y correlation of muon hits 5 cm upstream from the entrance window of TPC

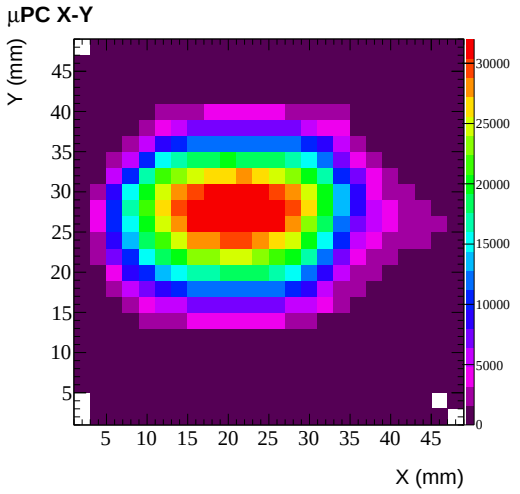

Figure 4: X-Y correlation of muon hits in the μPC.

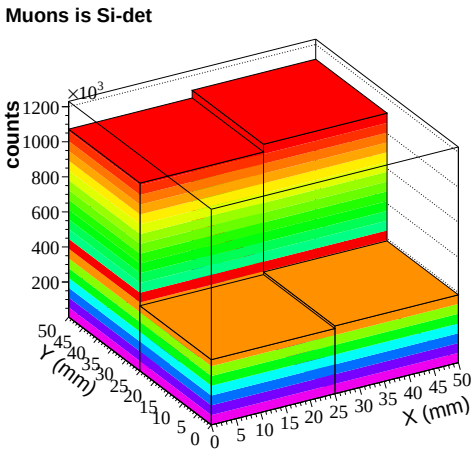

Figure 5: The distribution of muon hits in four quadrants of Si detector.

vacuum chamber is shown in Fig. 4. The beam was ~ 5.9 mm wide vertically and ~ 8.3 mm wide horizontally (RMS) suggesting good transmission of muons through the $R = 60$ mm entrance window of the TPC flange.

The X-Y distribution of muon hits in Fig. 4 indicates a slight off-centering of the beam vertically (by +2 mm) and horizontally (by -3 mm) with respect to the center of the μPC. However, the fraction of muons missing the entrance window of the TPC was unknown because it was difficult to establish the relative positions of the μPC and TPC in their working positions. Therefore, an additional muon detector was temporarily installed into the gap between μPC and TPC both for beam studies and to check the alignment of the TPC. This fourth detector was a thin (60 μm thick) square (5×5 cm^2) four-quadrant silicon detector. Its position relative to the TPC axis was well-defined because it was mounted directly to the front flange of the TPC vacuum chamber. The pulses from each of four 2.5×2.5 cm^2 quadrants were digitized by a dedicated WFD board for offline time and energy reconstructions. The energy information was used to distinguish between electrons and muons in the beam and the timing information was used to build coincidences with the μPC. As Fig. 5 indicates, the beam at the position of Si-detector indeed was slightly off-centered vertically while the horizontal position of TPC was very well adjusted. Thus, the measurements with Si-detector confirmed a small misalignment of TPC relative to the beam axis. Since the misalignment was small we decided not to interrupt data-taking for a new potentially disruptive re-survey of the apparatus.

3.3 TPC

The CryoTPC design used for runs R2010a and R2010b is shown in Fig. 6. The TPC vessel is a cylindrical shell with an outer diameter of 202 mm and a length of 360 mm which is machined from a solid piece of aluminum alloy. The walls of the shell have a thickness of 2.5 mm which is sufficient to sustain up to 15 bar pressure of hydrogen under cryogenic conditions. A beryllium window at one end of the vessel serves as an entrance for the muon beam. A new stainless-steel flange was installed at the other end. New high voltage feedthroughs (for 100 kV and 5 kV) provide a vacuum seal which is far superior to the original design. Both endcap pieces are joined with the shell by indium tooth-groove seals, which provide dismountable connections between heterogeneous materials with different hardness, such as

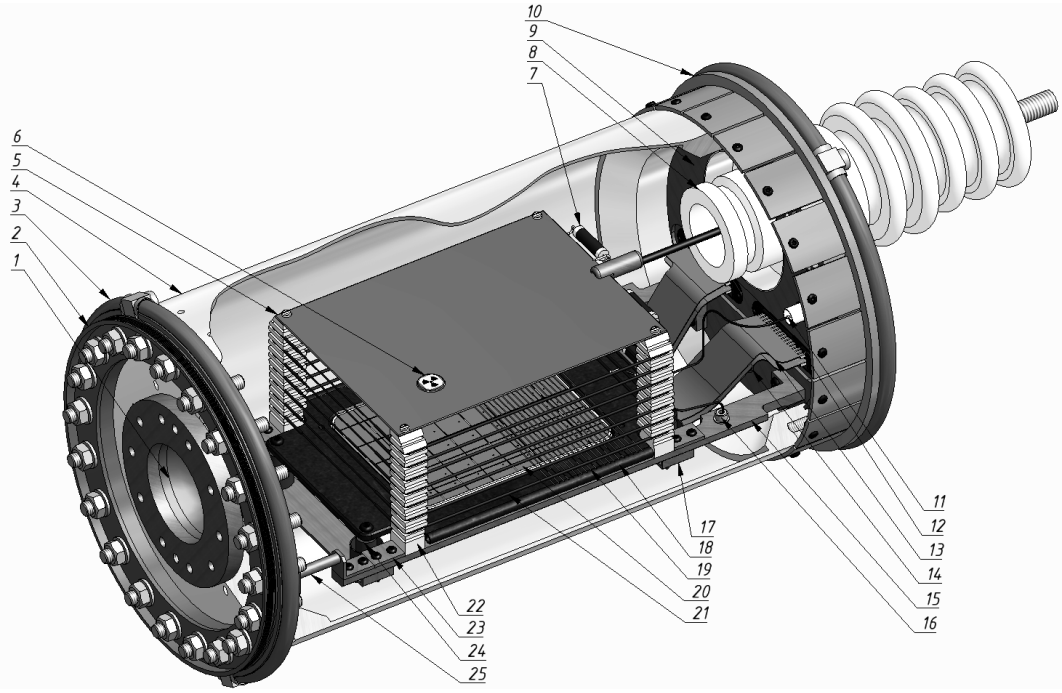

Figure 6: CryoTPC layout. 1 - Beryllium window, 2 - Heater, 3 - Front heat exchanger, 4 - Aluminum shell, 5 - Cathode, 6 - α-source, 7 - Dividing resistor, 8 - 100 kV feedthrough, 9 - Flange, 10 - Rear heat exchanger, 11 - 10 kV Feedthrough, 12 - 50-pin signal connector, 13 - Signal flat cables, 14 - Gas inlet, 15 - Supporting frame, 16 - Ground connection, 17 - Rear bracket, 18 - Grid frame, 19 - Grid wires, 20 - Pad plane, 21 - Potential-guiding wire, 22 - Stand, 23 - Front bracket, 24 - Grid insulator, 25 - Adjusting rod

stainless steel and aluminum. Unlike polymer seals, for example, the indium seal provides excellent containment under cryogenic conditions.

The detector is assembled on the flange and can be extracted from the shell in one piece. To support the detector, the flange has two stainless steel connecting bars which are rigid enough to support the weight of a high-voltage wire "cage" and the shielding grid (Fig. 6). The wires are connected in pairs by 10 kΩ resistors, forming the high voltage divider; the topmost wire is paired with the cathode and lowermost with the ground. The potential-guiding wires connected to the divider provide a uniformity of the electrostatic field in the cage at the level of 5%.

The massive Kovar frame of the shielding grid is fixed on four insulators which are supported by brackets. The insulators separate the grid, which is at 3 kV, from the grounded frame and unbiased pad plane. A grid of 20 μm tungsten wires is fixed on the frame by tin alloy with a 50 μm gap between wires. The frame has a mass of 400 g and is cut from 5 mm plate. Kovar is chosen to match the thermal expansion coefficient of the tungsten wires to prevent damage during temperature cycling.

The anode pad plane is made from a 2.5 mm MACOR slab (Fig. 7) with a copper layer and grid mask applied chemically to form 48 pads. The pad plane is glued to MACOR bars and attached to the grid to form a single assembly. The pads are read out on the side opposite the drift region through low-capacitance Kapton flat cables.

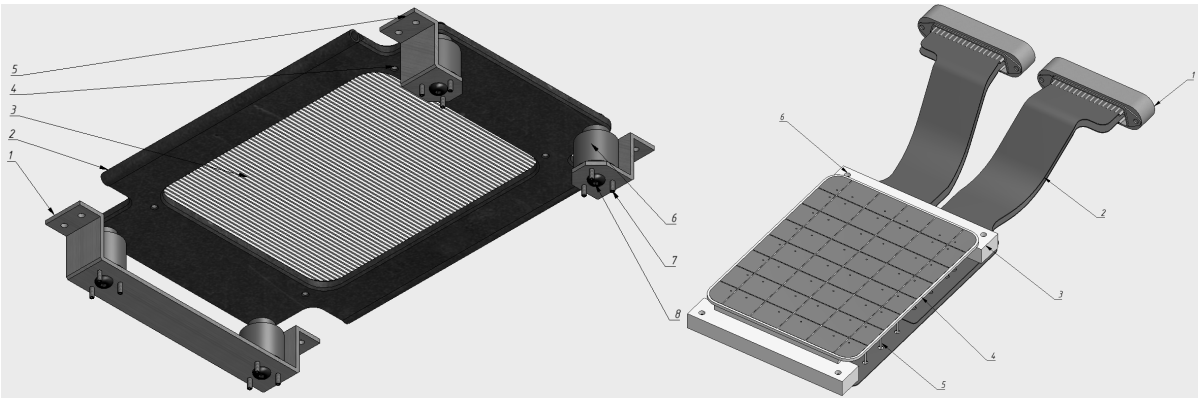

Figure 7: **Left: Shielding grid** 1 - Front bracket, 2 - Kovar frame, 3 - Tungsten wires, 4 - Connection holes for pad structure, 5 - Rear bracket, 6 - Insulator, 7 - Adjusting screw, 6 - Fixing screw. **Right: Pad structure** 1 - 50-pin connectors, 2 - Flat cables, 3 - Bar, 4 - Pad plane, 5 - Pin, 6 - Connecting hole

3.4 Cryosystem

During spring 2010, the cryosystem was tuned up to working conditions, with further improvements throughout the year in preparation for the R2010a and R2010b data runs. Cooling of the TPC is accomplished with liquid neon circulation from a cold head and condenser through copper pipes around the TPC vessel. The cold head is connected with a massive copper condenser which has a number of vertical lamellas to increase the heat transfer surface (Fig. 8). A thin indium foil is used to provide better heat contact between the cold head and the condenser. Control of the condenser temperature is accomplished with an electrical heater. The lamellas of the condenser are hermetically cased in a condensing shell which has four 12 mm copper pipe input and output connections. Approximately 0.5 m below the condensing cell, the copper pipes are coupled with flexible bellows in pairs with the rear and front heat exchangers of the CryoTPC. The cooling manifold is connected with a 40 L reserve volume (not shown in the scheme) and filled with neon up to 5 bar at room temperature.

During operation, the cold head cools the condenser with the maximal cooling power, while a heater provides fine temperature adjustment. Liquefied gas forms on the lamellas of the condenser and drains down to the bottom of the condensing shell and into the copper pipes. Liquid neon flows through the bottom pair of bellows to the TPC head exchanges, where it evaporates, returning to the condenser in the gaseous phase through the upper pair of bellows Thus, an unforced circulation loop of neon is formed in the cooling manifold.

Due to very limited cooling power of the cold head at working conditions, protecting the system from environmental heat transfer is essential. This is accomplished by a conventional set of technical solutions. A high vacuum ($2 - 4 \times 10^{-7}$mbar) insulation vessel encases all cold components, including the TPC vessel. Aluminized Mylar shielding in 3-4 layers covers all components inside the insulation vacuum to reflect infrared radiation. Also, heat bridges are used to minimize conductive thermal transfer where mechanical parts are connected.

The inner TPC vessel is supported from the downstream side on four thin-walled stainless steel tubes. The rods are connected to the base supporting flange of the vacuum vessel and bear most of the CryoTPC mass. To give the suspension additional rigidity, the upstream side of the detector has three threaded rods connected with the endcap by a special flange.

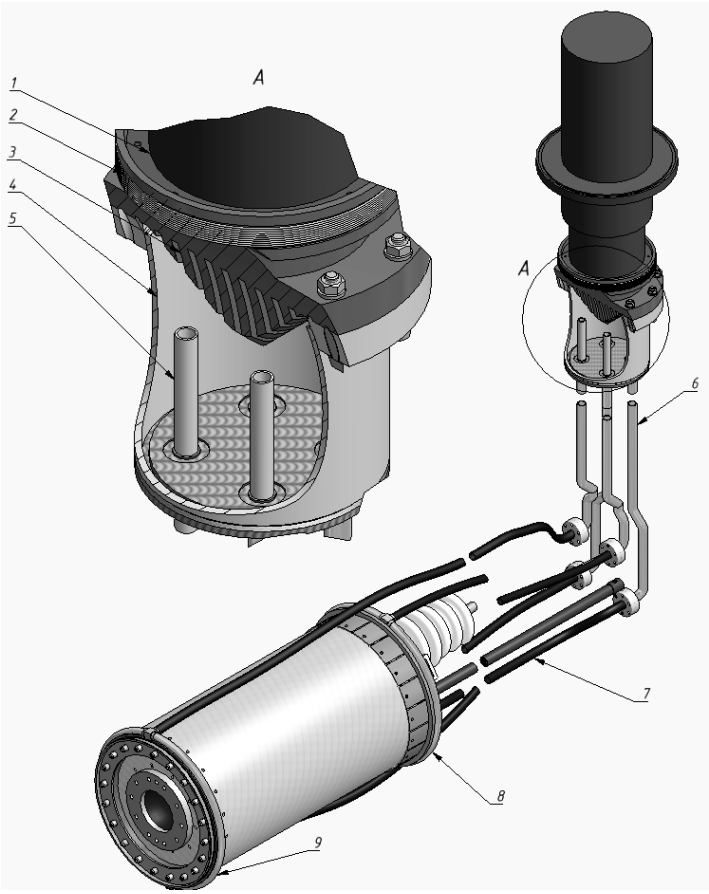

Figure 8: Cooling Apparatus. 1 - Cold head, 2 - Heater, 3 - Condenser, 4 - Condensing cell, 5 - Gas return pipe, 6 - Copper pipes, 7 - Bellows, 8, 9 - Heat exchangers

3.5 Electron Detectors

The muon decay electrons are detected with a barrel hodoscope around the TPC consisting of a double layer of scintillator for fast time resolution and two multi-wire proportional chambers for tracking. The scintillator "gondolas" are 0.5cm thick, arranged in 16 telescopes of two layers each, and read out at both ends by threshold discriminator and waveform digitizer. The two wire chambers each have an anode plane sandwiched by two opposing helicity cathode strip planes. The cathodes are read out in addition to the anodes in order to provide two dimensional position information. All wire chamber signals are amplified and sent through a threshold discriminator to TDC modules. Full electron tracks are used for the lifetime analysis, consisting of coincident hits in multiple planes of each wire chamber and a 4-fold coincident hit in both readout ends of a gondola telescope.

Following the repair of one of the wires of the larger wire chamber from its use in the MuCap experiment, the chambers were reassembled and trained to full high voltage in February 2010. Additionally, it was necessary to perform a realignment calibration of the wire chambers relative to each other, the gondola scintillators, and the TPC. This study was accomplished with the use of a dense target and a μ^+ beam as well as with cosmic particles.

During the R2010b data run, extensive effort was made to suppress noise in the chamber, especially in the cathode strip readout. Geometrically, the induced signal is split between multiple cathode strips on both planes, so the signal to noise ratio is worse than on the anodes, and noise suppression is all the more important. In the R2010b run, the cathode

amplifiers were found to pick up a periodic signal from the digitizers. While the discriminator thresholds can be set above the pickup, the effect persists, and examination of the auto-correlation of cathode hits shows this periodicity. Some basic shielding attempts were made during the run, but time will be devoted to suppressing this pickup before the R2011 run.

Another problem is that the LVDS drivers in the readout circuits for the cathodes have a tendency to oscillate when not connected, and one bad channel induces oscillation in all channels on the same circuit board. Because the connectors have aged over many years of use in the MuCap experiment, the cable connection pins do not make good contact, leading to oscillation. Replacing the output pins on these circuit boards was found to dramatically reduce the oscillation, greatly improving the number of stable, active channels on the chambers. Changing the pins on every one of the boards is not currently necessary, as the problematic boards can be individually identified and fixed.

3.6 Neutron Detectors

Muons in deuterium yield two sources of neutrons: (i) fusion neutrons following $d\mu d$ molecule formation and the subsequent $dd\mu \rightarrow^3 He + n + \mu$ fusion reaction, and (ii) capture neutrons following the $\mu d \rightarrow n + n + \nu$ capture reaction from the muonic deuterium $F = 1/2,\ 3/2$ hyperfine states. The $d\mu d$ fusion neutrons are mono-energetic with energy 2.45 MeV. The two coincident neutrons from μd capture have a continuum energy spectra that peaks at 1-3 MeV and extends to 53 MeV.

Encoded in the time dependence of the fusion neutrons are the two $d\mu d$ molecular formation rates from the $F = 1/2,\ 3/2$ hyperfine states (Λ_{dd}^{Q} and Λ_{dd}^{D}) and the hyperfine transition rate (Λ_{qd}) from the higher-energy $F = 3/2$ state to the lower-energy $F = 1/2$ state. Consequently, the detection of fusion neutrons will enable the determination of the kinetic parameters Λ_{qd}, Λ_{dd}^{Q} and Λ_{dd}^{D}, which are important in the extraction of the μd doublet capture rate, Λ_D, from the measured decay-electron time spectrum.

The detection of μd capture neutrons is more challenging due to their low yield of roughly 10^{-3} per muon stop and their low energies of typically 1-3 MeV. However, the time spectrum of μd capture neutrons offer the possibility of both a cross-check of the aforementioned hyperfine transition rate (Λ_{qd}) and a determination of the hyperfine capture ratio (*i.e.* the ratio between the μd capture rates from the quartet state Λ^Q and the doublet state Λ^D). Again, these quantities are important in the extraction of the μd doublet capture rate, Λ_D, from the measured decay-electron time spectrum.

Installation of the eight-detector array of liquid scintillator neutron counters was early in the R2010b run. The neutron counters are cylindrical cells of 13 cm diameter by 13 cm depth and contain approximately 1.2 liters of BC501A organic scintillator. The cells were coupled to 13 cm diameter photo-multiplier tubes and read out by eight channels of 12-bit, 170 MHz custom-built waveform digitizers. After establishing the energy calibration and neutron/gamma-ray discrimination with radioactive sources the neutron counter array was successfully operated for the R2010b run.

Neutron analysis goals from the R2010b run include: (i) the further development of the neutron analysis framework for the MuSun experiment, (ii) studies of the 2.45 MeV neutrons from the $d\mu d$ fusion reaction to determine our sensitivity to the fusion rates (Λ_{dd}^{Q} and Λ_{dd}^{D}) and hyperfine transition rate (Λ_{qd}), (iii) studies of the low-energy neutrons from the μd capture reaction to determine our sensitivity to the hyperfine transition rate (Λ_{qd}) and the hyperfine capture ratio (Λ^Q/Λ^D), and (iv) and studies related to maximization of signal rates, minimization of background rates, and optimization of instrumental resolution and neutron/gamma-ray discrimination.

As an example of the ongoing analysis effort on the R2010b neutron dataset, Fig. 9 shows

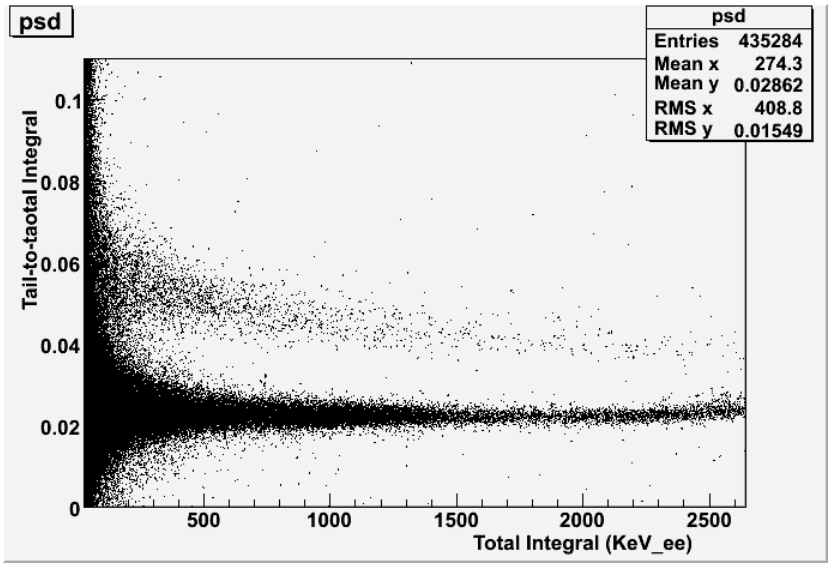

Figure 9: Sample plot of the tail-to-full amplitude ratio (vertical axis) versus the full amplitude (horizontal axis) for one neutron counter. The strong lower band corresponds to gamma-rays that produce a small fraction of slow-component scintillation light. The weaker upper band corresponds to neutrons that produce a larger fraction of slow-component scintillation light. At electron-equivalent energies above 4000 keV the n/γ discrimination is degraded as pulses exceed the range of the waveform digitizers.

the neutron/gamma-ray pulse-shape discrimination for the eight neutron counters. The pulse-shape discrimination is based on the difference in the length of the pulse tail for neutrons or gammas. The ratio of the slower component of scintillation ligth to the total pulse amplitude separates the particles into two bands. Fig. 9 plots the distribution of full pulse amplitudes (horizontal axis) to pulse tail amplitudes (vertical axis) and shows the separate bands from neutron signals and gamma-ray signals for energies exceeding $\sim$0.5 MeV.

Presently, a Kentucky graduate student is working on the analysis of the neutron dataset to extract the distribution of the time between muon stops in the deuterium gas and neutron signals from both the $d\mu d$ fusion reaction and the μd capture reaction. This analysis requires the application of cuts to (i) distinguish the muon stops in the D_2 gas from muon stops in surrounding materials and (ii) distinguish the fusion neutrons, which are accompanied by a delayed electron, from the capture neutrons, which are not accompanied by a delayed electron. In addition, to optimize the signal-to-background ratio a careful detector-by-detector determination of the energy calibration and optimization of the neutron/gamma-ray discrimination is required.

4 First Analysis of 2010 Data

4.1 Analysis Framework

The MuSun data analysis software is built on the existing MuCap analysis code which is written largely in C++, incorporating both MIDAS and ROOT libraries. A multi-stage processing model is employed in order to separate processing that needs to be performed once or infrequently, such as pulse finding, from processing that must be repeated often, such as ongoing development of a track-finding algorithm. In the first stage, raw detector signals are processed to construct physical objects - like muon pulses, electron tracks, or neutrons - which

are stored in ROOT's tree format. Later stages then utilize these base objects to construct higher level objects, such as muon-electron decay pairs. Cuts are applied to these higher level objects to extract the muon lifetime and also to discover and analyze systematic errors. Splitting the computation into stages allows an expedient reprocessing of higher level objects without forcing an additional computationally intense pass over the raw detector signal data.

Many of the basic MuCap processing modules are directly portable to MuSun, since MuSun employs the same electron and neutron detectors as MuCap, but the TPC pulse finding and muon track finding algorithms require independent development. The TPC analysis in MuSun differs from that of MuCap in several ways: MuSun has full analog readout, rather than just the discriminated signals of MuCap, the topology of the readout plane differs, and charged fusion products in the deuterium environment present a source of signals correlated in time with the muon signal. In order to handle these experimental novelties, the collaboration is putting considerable ongoing effort into the development of a muon stop identification that is robust against time-dependent systematic effects. Emphasis is put on exploring several different algorithms for TPC pulse fitting and muon tracking with the goal of comparing the strengths and shortcomings of each. Software development is focused on facilitating the independent development these different algorithms and incorporating them efficiently into the code base.

The second stage in the analysis is a modularized framework that allows for separate analysis of diverse physical information such as the muon lifetime, neutron spectra, or fusion recoils. This stage passes over the ROOT tree output from the first stage forming correlations between basic objects, such as the construction of a muon track from muon pulses, or decay events from muon-electron coincidences. Since this stage requires considerably less processing than the first stage, it is practical to run frequent passes with refined cuts and spectra. While developing a particular analysis, such as muon track-finding, the processing is done at this level, where frequent reprocessing of the data is fast. As such algorithms converge and the processing becomes standardized, they are migrated to the first stage processing, maintaining the lightweight flexibility of the second stage.

Besides general developments on the analysis, we also have developed customizable event displays in order to study specially selected events by eye. The graphical representation of typical and very special muon tracks in the TPC and their topologies is an essential tool for developing the new muon stop definition. Especially in the initial stages of analysis, the event display is regularly utilized in evaluating the general attributes of single events as well as verifying the efficacy of the analysis algorithms.

4.2 TPC Signals

The CryoTPC plays a central role in cleanly measuring the 3 dimensional stopping position of the incoming muons, observing the reaction products of the muon catalyzed fusion branches $dd\mu \rightarrow {}^3He + \mu$ and $dd\mu \rightarrow p + t + \mu$, and monitoring nuclear recoils of typically some 100 keV, resulting from muon capture on trace impurities. The properties of these signals and the recorded energy/charge is shown in Tab. 2. With no gas amplification at the high D_2 density of $\phi = 0.06$, signals are small and electronic noise minimization and optimal signal processing is essential. The signal to noise situation achieved in R2010b can be best studied with a so called forced trigger, i.e. the WFD readout is triggered on all channels for 18 μs after a prescaled entrance counter signal. A typical event display shows clear signals from the incoming muon, the general noise level, as well as RF pickup and small high frequency oscillations in the WFD input. Apart from the minor last effect, they determine the signal resolution and might enter the systematic lifetime distortions at higher order. The ongoing resolution studies are discussed in section 5.

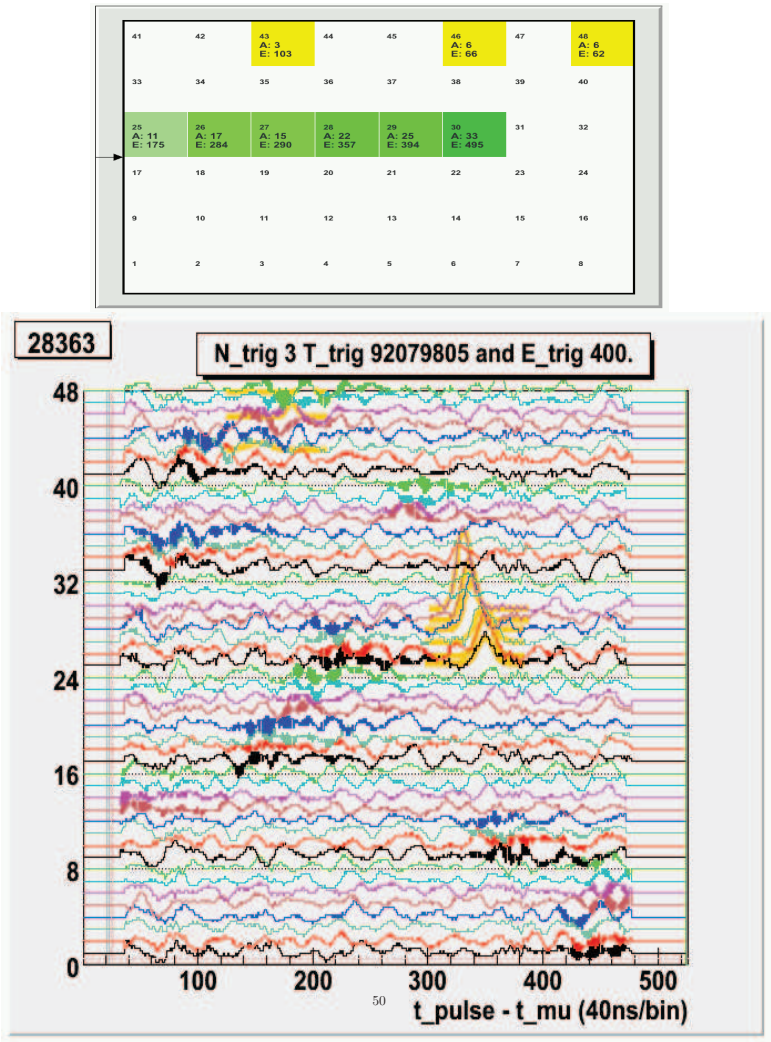

Figure 10: A sample forced trigger event with a muon stop. All WFD channels trigger for the full drift time of 16 μs. The orange pulses show the gaussian fit to the muon track pulses.

While the forced trigger gives the most complete information on the event, the high muon stop rate allows only selected islands around threshold-triggered WFD pulses to be recorded. In R2010b, stable triggering right above the noise level was achieved with digital WFD thresholds, well within the DAQ bandwidth of ∼15 MB/s. Fig. 11 shows the recorded pulses as well as a simple pulse analysis based on Gaussian fitting. This works well for the nearly horizontal tracks of incoming muons, where the drift charges arrive simultaneously at the anode pads. For tracks with vertical components y (in mm) the signal width gets extended by $\approx 200ns \times y$. For fusion events including $p + t$ recoils, this fit completely fails, see Fig.11, rhs. Improved algorithms to optimize the energy resolution and properly account for the more complex fusion topologies are under development.

Once the pulses have been identified, the second stage of the analysis chain identifies tracks and clusters. Again the optimization of this algorithm is a key challenge for MuSun and several complementary methods are under development. Different from normal tracking in a particle detector, the emphasis is on avoiding time dependent interferences, which would distort the lifetime at the few ppm level. A simple-minded muon stop finder was used online during the run, requiring two pads with large energy deposition along the track. Fig. 12 shows

	E (MeV)	E_{obs} (MeV)	Q (fC)	R(mm)
μ *)	0.2-1.2	0.2-1.1	0.9-4.8	
^{3}He	0.82	0.6	2.6	0.18
μ^3He	0.80	0.75	3.3	0.6
t	1.01	0.9	4.0	1
p	3.02	2.8	12.3	16

Table 2: Recoil energies and range of fusion products at ϕ=0.06. The observed energies are lower due to charge recombination. The deposited charge assumes 4.4fC ionization charge per MeV energy deposition in hydrogen. *) typical range of muon energy deposition on pads.

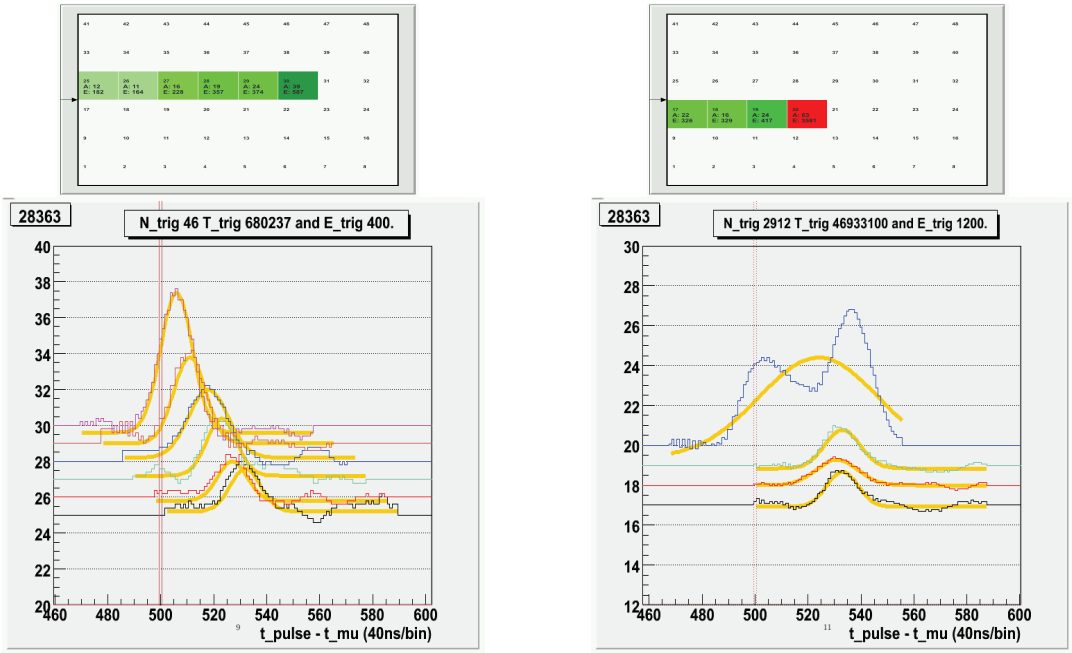

Figure 11: Muon tracks showing the pulse fit function. On the left, all pulses are fit well. On the right, the track of the proton-triton fusion products is fit poorly with a Gaussian. The vertical line is only the event display trigger time; it indicates nothing physical.

the resulting stopping distribution, which indicates good containment of the muons stops in the TPC volume. The present estimate of 50% TPC stops per entrance counter signal is a rough estimate only and requires more analysis work.

The rather spectacular signals of delayed $p + t$ fusions are shown in Figs. 1 and 11, rhs. The triton stays at the muon stopping position, while the proton ranges out in 16mm, or about one pad length. If the proton has a vertical velocity component, its energy deposition characterized by the Bragg curve is clearly visible as function of drift time. Muon catalyzed fusion events play a dual role in this experiment. On the positive side, they serve as a powerful monitor to prove that the muon kinetics is quantitatively understood. The ^3He recoil also provides a local, well defined energy deposition. Once selected delayed relative to the muon stop pad, it can calibrate the energy scale and determine the resolution of the chamber in-situ during the run. On the negative side, interference between fusion and muon stop identification has to be scrupulously avoided. As the fusion signal indicates that the muon has lived at least up to the moment of fusion, the time distribution of electrons with a fusion requirement is different from the pure exponential of electrons after muon stop. Different strategies to make

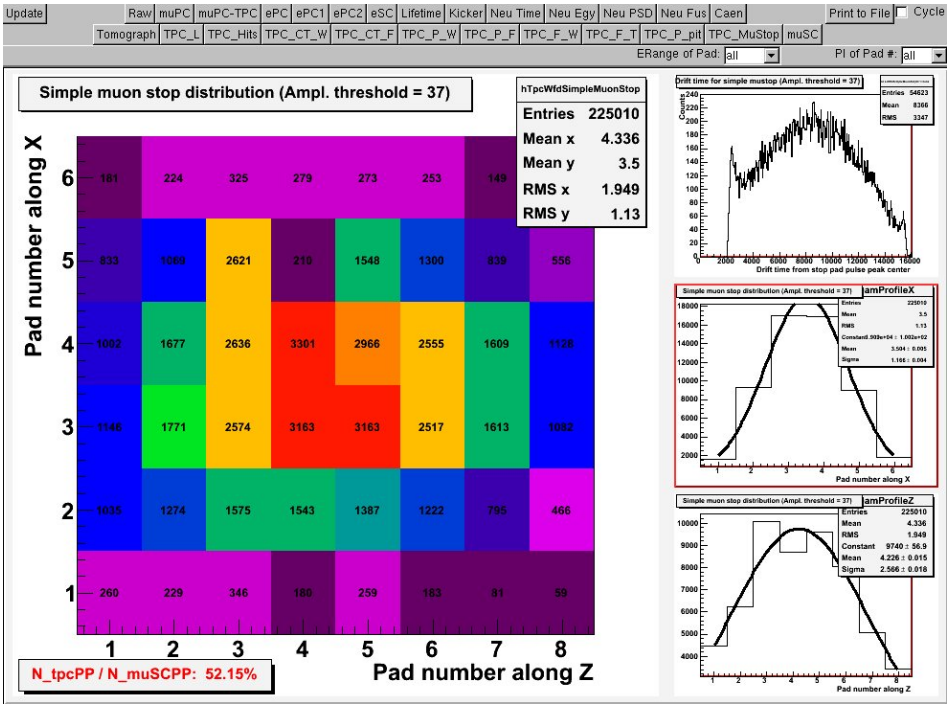

Figure 12: Online display of the TPC. Stops per pad is shown on the left. The plots on the right are, from top to bottom, the drift time distribution of muon stops, the horizontal stop profile transverse to the beam, and the stop profile along the beam direction. Many different customizable displays exist for examining all detector systems as well as online quality checks.

the mustop finder insensitive to fusion are being explored, including basing it on upstream pads, which cannot be reached by recoils, as well as trying to simply rely on a low energy threshold. In the latter case, additional energy deposition due to fusion will not affect the number of accepted muons. Dedicated Monte Carlo studies, including the noise and detector responses established in the R2010b run, are being prepared. Monte Carlo can generate events with 100% fusion per mustop, while this fraction is only 5% at our experimental conditions.

4.3 Electron Time Spectra

The data in run R2010b provides the first opportunity to thoroughly explore the quality of fits to the muon lifetime with a statistics of about 10% of the full expected data of the MuSun experiment. In Fig.13, one can see the muon lifetime fit for a few runs, amounting to 2×10^7 μ^+ decays and 6×10^7 μ^- decays. The μ^- spectrum shows an initial high-Z capture component to the lifetime, while the μ^+ decays with the free muon lifetime. By requiring a muon stop in the TPC, the μ^- spectrum is cleaned of this component. The full R2010b data will be analyzed, once several complementary pulse finder and tracker strategies have been sufficiently developed, with selection criteria optimized to avoid systematics distortions of the lifetime fit.

4.4 TPC Operating Range

The CryoTPC was operated at 32K and 6% liquid hydrogen density during the data-taking portion of the R2010b run. The collaboration was interested in exploring the feasibility of operating the TPC at a higher density for future data runs. While the CryoTPC was designed to operate at 6% density, the system is capable of supporting higher densities. Thus, after

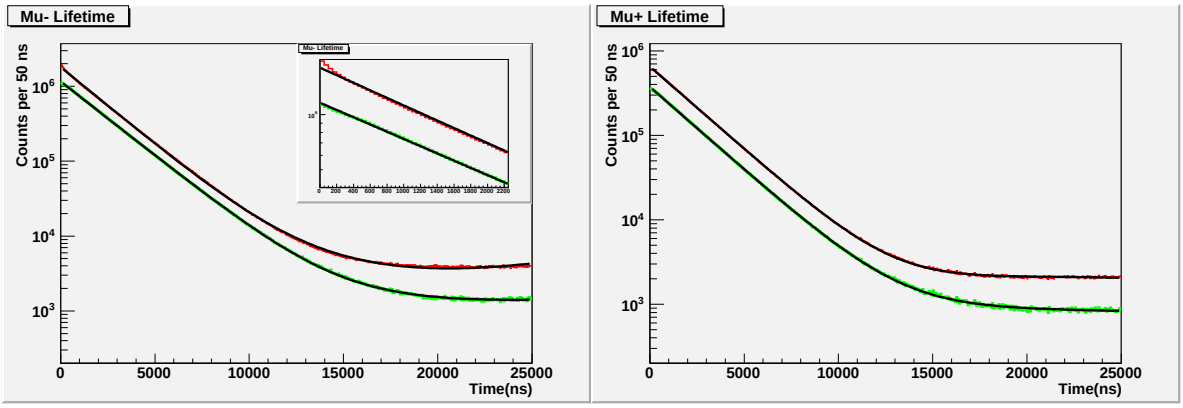

Figure 13: Fits to the electron decay spectrum for μ^- (left) and μ^+ (right). The red curve is the spectrum for all muon-electron pairs and the green curve is the same spectrum with the additional requirement of an identified muon stop in the TPC. Inset expands the early time region to highlight the high-Z capture component of the muon lifetime.

concluding data accumulation, a volume of deuterium was added to the TPC in order to increase the gas density to 11%. To avoid deuterium condensation at the required 9.5 bar pressure, the temperature was raised to 37K. At a higher density, the quartet to doublet depopulation rate is increased, which causes fusions to occur more promptly after the muon stop. It is possible that this condition would allow avoidance of systematic effects from the fusion products in the TPC simply by starting the lifetime fits later after the muon stop. Moreover, higher density also has the effect of raising the energy deposition per pad for muons, increasing pulse sizes relative to the electronic and acoustic noise. Since the fusion products are nearly localized to a single pad by their short range, the size of the fusion pulses would remain constant or decrease from ionization recombination effects.

The results were surprising and visible even with the online diagnostics from the counting room. As the density increases, the electronic drift in the TPC was quenched for signals originating higher in the chamber. As an example, the so-called "S-energy" was used as a diagnostic tool. The S-energy is the energy deposited in the last pad in the muon track plus half the energy deposited in the next-to-last pad. Empirically, it is found that this quantity is well-peaked due to the muon Bragg curve and pad dimensions. Fig. 14 shows a plot of the S-energy against the drift time of the signal, relative to the muon entrance time. In principle, the S-energy should not be strongly geometry dependent, and certainly not vertically asymmetric. The observed phenomenon is unknown to the collaboration and a cursory literature search provided little elucidation.

Without knowing the mechanism for the signal loss, data was collected with the hope that an extensive data set could provide an explanation. Since the drift velocity of ionization electrons is dependent on the gas density and chamber drift field, several small data sets were taken at densities from 6% to 11% and drift cathode voltages from 20kV to 100kV. Extensive followup analysis of this data has not been performed as of this report.

5 Systematics Issues and Improvements

5.1 Purity

The effect of contaminants on the $\mu + d$ capture rate Λ_d put very stringent demands on the purity of the deuterium gas used in the measurements. Collisions of μd atoms with higher-Z impurity atoms, followed by muon transfer and subsequent capture, will produce a direct

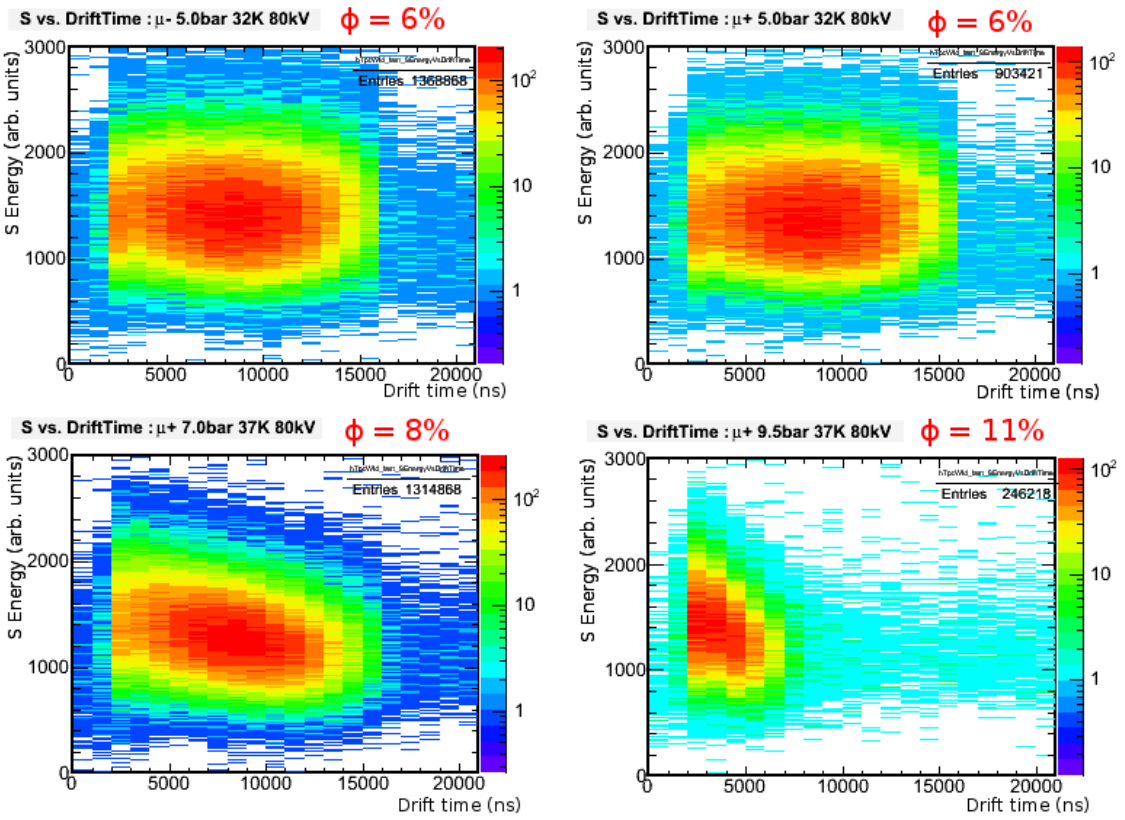

Figure 14: Diagnostic plots of the muon S-energy vs. signal drift time. Top row: Nominal density condition for μ^- and μ^+. Bottom Row: Density increased to 8% and 11%, μ^+ beam, with the signals higher in the TPC (larger drift time) disappearing.

systematic increase in our measurement of Λ_d. The large rate for muon capture on higher-Z atoms requires that such impurities be reduced to the ppb level or less. As outlined in the proposal, reducing the systematic shift $\delta\Lambda_d$ to $\sim$2 Hz requires that nitrogen contamination levels be less than 1 ppb.

Protium gas is also a concern. The formation of $p\mu d$ molecules followed by the fusion reactions $p\mu d \rightarrow \mu^3$He(85%) or $p\mu d \rightarrow \mu$(5.3MeV)+^{3}He(0.2 MeV)(15%) lead to a systematic increase of Λ_d. The second channel (which produces 5.3 MeV Alvarez muons) is more dangerous, since it can eject the muon into the target walls. A residual content $c_p = 100$ ppm leads to a change $\delta\Lambda_d$=$\sim$2 Hz.

5.1.1 CHUPS system

The CHUPS [21] system is used for maintaining chemical purity and stable pressure inside the TPC during experimental runs. Apart from the occasional replacement of stainless steel cartridges in the mechanical filters, the system requires no maintenance. These new cartridges provide stable 3-slpm flux of the working gas at stable pressure. At the end of two months continuous running this fall, the internal humidity sensor indicated that contamination from water vapor was less than 0.1 ± 0.1 ppb. The effectiveness of the CHUPS system was demonstrated again at the end of the R2010b run, when the TPC was brought to room temperature and there was no significant increase in water vapor.

The chemical purity of the gas, specifically the levels of O_2 and N_2 contamination, was monitored using the chromatographic technique described in [21]. One significant improve-

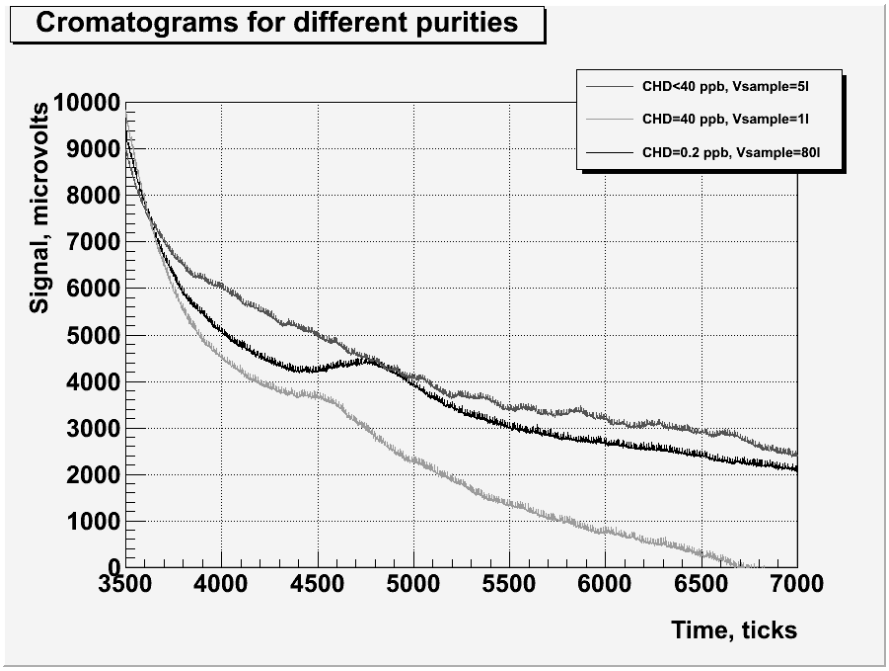

Figure 15: Chromatograms (response of the thermal conductivity sensor to analyte as a function of the retention time) for various sample volumes and concentrations.

ment in our technique was to connect the sampling line of the chromatograph directly to the TPC outlet with a stainless steel capillary. The new technique, which allows us to probe volumes as large as 80 liters, reduces sampling errors. Examples of chromatograms for various sample volumes and concentrations is given in Fig. 15. Our best result was registered at the end of the R2010b: 0.2 ppb for N_2 and < 0.2 ppb for O_2.

5.1.2 Isotopic purity

The principal achievement in 2010 was the chromatographic measurement of the HD fraction in deuterium of high isotopic purity (better than 99.9%). A LHM-8M chromatograph was adapted to measure the concentration of HD molecules in deuterium. The separation is done in a column filled with a mixture of Al_2O_3 and Fe_2O_3 held at 78 K, by means of a liquid nitrogen bath. Neon is used as a carrier gas; the detector is catarometer, or heat conductivity detector. The probe of deuterium is injected into the chromatograph by the sampling valve. The operator waits until the first peak (HD) is completely out and painted on the chromatograph PC screen as a vivid Gaussian-like peak, then switches the amplifier to low gain mode. Usually the amplification factor between "high gain" and "low gain" is 50-100. The operator then waits for the next peak (D_2) and completes the registration. Unless the concentrations are different by more than a few orders of magnitude, switching the gain allows the operator to make comparable the area of the peaks. Having the peaks of comparable area clarifies the subsequent interpretation of the chromatogram. A typical chromatogram of deuterium with a small admixture of HD molecules is given in Fig. 16. This chromatogram corresponds to a sample taken from the CryoTPC during the fall run. Since HD has a lower affinity for the chromatographic adsorbent than D_2 it leaves the column first (left peak on the figure, highlighted in blue). Note that the areas of the peaks depend on the probe volume, but the ratio of the areas does not. Thus, larger volumes reduce the sampling error and therefore are preferable for the analysis.

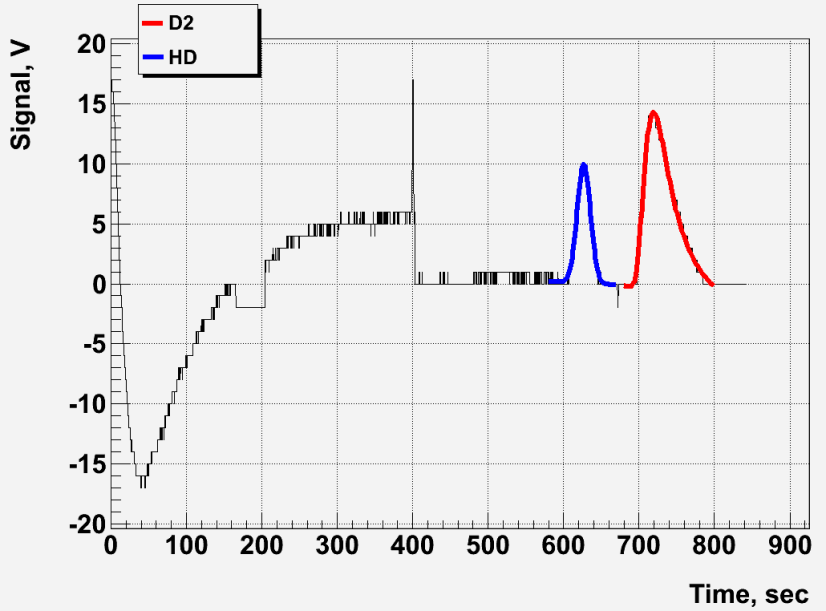

Figure 16: Typical chromatogram for a sample from CryoTPC in R2010b. The left peak (blue) corresponds to HD, the right peak (red) corresponds to D_2. Note that the chromatograph was switched from "high gain" to "low gain" at $t \approx 670$ s.

The composition of the mixtures was determined using a so-called method of internal normalization. According to the method, the concentration C_i of the component i in a multi-component mixture was calculated in mole fraction by the formula (2)

$$C_i = \frac{S_i k_i}{\sum_{j=1}^{i} S_j k_j} \tag{2}$$

where k_i is individual coefficient of the component i, S_i is the area of the peak corresponding to the component i. The individual coefficients k_i are constant to the species and do not depend on the pressure or the type or exemplar of catarometer. They are normalized by a coefficient $k = 1$ for a standard gas which is hydrogen in the particular case. The individual coefficients were measured at PNPI to be $k_{\mathrm{HD}} = 1.35 \pm 0.01$, $k_{\mathrm{D_2}} = 1.74 \pm 0.03$ using pure (better than 99.9%) components, H_2, D_2, HD. The proposed chromatographic method is capable to measure the HD concentration in deuterium down to at least $0.026 \pm 0.004\%$.

5.2 TPC Noise Performance

Several improvements of TPC readout have been made in the electronics and digitization. Pickup from the temperature sensors and heaters of the cryogenic system has been eliminated. The front end field transistor of the preamplifiers has been exchanged for one with a larger transconductance, diminishing the intrinsic noise. In the 2010b run, the vibration of the cold head compressor was found to cause the charged grid wires to induce a 600 Hz signal in the TPC pads. As this acoustic frequency is small compared to the muon decay rate, the effect is seen as a slow base-line shift of the TPC signals. For the R2010b run, the amplifiers were fitted with a high-pass filter of exponential time constant $\tau = 40\mu$s in order to suppress the acoustic vibrations by a factor of 20 (see Fig. 17). For the R2011 run, installation of base line restorers will suppress the acoustics by a factor of 50.

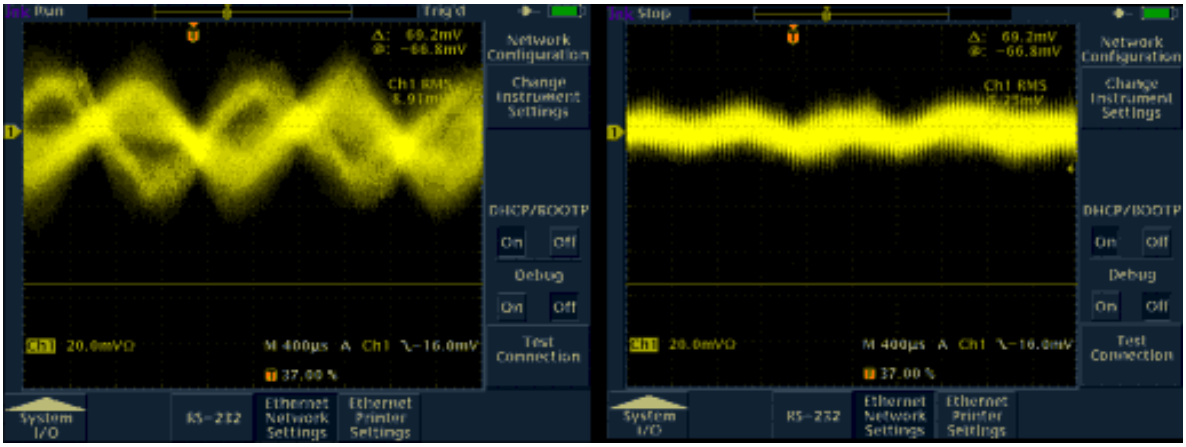

Figure 17: Scope pictures: Left - before the acoustic noise suppression, Right - after the suppression via high-pass filter.

At the same time, several "smarter" triggers have been developed for the WFD. The first trigger, implemented on some test modules towards the end of the R2010b run, addressed the trigger problems associated with brief, periodic bursts of high frequency ringing. To reduce the impact of the ringing, the trigger was derived from an average of the signal over a selectable interval. Following the same spirit, the baseline was established from a (longer) selectable window. In a more recent firmware, released since the end of run R2010b, a low-pass digital filter is used to select out the slowly changing baseline. The trigger decision is then based on a suitably averaged signal with that baseline removed. The advantage of triggering with the aid of the digital filter is that the data itself is *not* changed in any way and is therefore less likely to introduce distortions into the exponential lifetime fit.

Sparks are another issue under consideration. High voltage discharges in the insulation vacuum cause large signals in the TPC readout electronics, as seen in Fig. 18. The baseline drops back to normal after about $20\mu s$ and the frequency of the sparks is on the order of 1Hz, so cutting the data segments with a spark in the TPC represents a small loss in data rate. However, it is possible the baseline is shifted by a small amount for much longer than the duration of the spark, which would be a time-dependent systematic effect on the muon detection threshold. A study will be conducted of the effect of the proximity of a spark on the muon lifetime to determine the magnitude of such an error.

5.3 Summary systematic improvements

Several improvements are dependent on ongoing analyses combined with software developments, and we will learn more as those analyses advance. This include resolution, track finding and fusion interference, impurity detection and TPC sparking. Those will effect the hardware upgrade proposed for MuSun as shown in table 3. The urgent upgrades before next run in 2011 will take place in May and June. Further thoughts on longer term upgrades, possible during the commissioning of the new $\pi E1$ area in 2012 are also indicated.

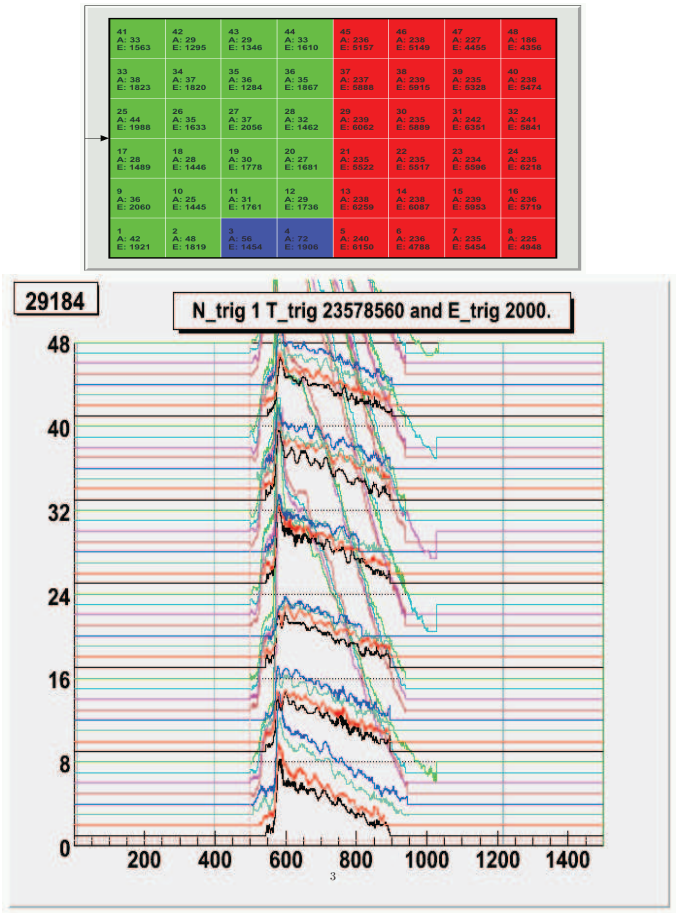

Figure 18: A discharge of the cathode voltage in the insulation vacuum. The time scale is in clock ticks, which are 40ns. The pickup signal from the sparks lasts up to $20\mu s$.

System	**Task**	**before R2011**	**after R2011**
Area	Commissioning new $\pi E1$ area		2012
TPC	Generation D_2 with high isotopic purity	May 2011	
	New grid and thick gold plated pad plane	May 2011	
	New Impurity Concentration System (ICS)	June 2011	2012
	Improvements high voltage system, baseline restorer	May 2011	
	Final improvement of high voltage system, acoustics		2012 *)
	In vacuum cold preamplifiers		2012 *)
	Optimized pad geometry		2012 *)
	Capture signal detection and dedicated pure H2 run		2012
	Improved isotopic purity monitoring		2012
ePC	Replacement cathode cards	June 2011	
neutron detectors	Deploy large DEMON detectors		2012 *)

Table 3: Planned MuSun hardware upgrades separated in before and after run 2011 (**R2011**). (*) If required by run 2011 experience and analysis.)

6 Plans and Beam Time Request 2011

2011 will be an important and exciting year for the MuSun experiment. In various aspects we want to improve and finalize the experimental setup which was already successfully operated last year. Based on the experience gained during the first production-quality run in fall 2010, we plan to fine-tune the hardware, analyze the detector performance achieved, and perform all necessary upgrades where problems were identified. We will run the MuSun detector with muon beam during three cycles (12 weeks) of beam time in summer 2011. This will be the final MuSun production run in area $\pi E3$. Our main goal is to produce a improved measurement of the $\mu + d$ doublet capture rate with a statistics of about 10^{10} good events and publish it as the initial MuSun result. For systematics reasons, part of this data will be taken with μ^+ beam and other parts under special conditions. In the following brief sections, we outline the collaboration's work plan and summarize our beam request.

6.1 Collaboration Plans and Tasks

- **Improvements of MuSun electron wire chamber system**. The cylindrical wire chamber system consisting of ePC1 and ePC2 performed smoothly in fall 2010, after aging preamplifier cards had been replaced by spare cards during the run. Additional redesigned cards are required and will be produced and installed before the run.

- **CryoTPC system**. In May 2011 the PNPI team will arrive. In a first job, the cold box of the Neon refrigeration system will be dismounted from the CRYO-TPC stand and installed on our isotope separation facility. Then the deuterium of all our inventories (∼5'000 stp liters) will be purified to a depletion level below 0.01% protium, sufficient to avoid any systematic corrections due to formation of pμd molecules. This purification is required, because our present deuterium contains about 0.2% protium in the form of HD molecules.

  In parallel work, the 80kV HV system of the TPC will be assembled and improvements tested to reduce sparking which still affected the efficiency and quality of the 2010 run.

  After finishing the isotopic purification job, the complete CryoTPC system will be assembled and tested under full experimental conditions. The task list for these tests includes:

  May
  Modification of various elements of the high voltage system.
  Vacuum and cryogenic tests with the upgraded HV elements.
  Installation of new grid and MACOR pad plane into CryoTPC.
  Installation of new Kapton flat cables.
  Cleaning CHUPS.
  Testing the new cryogenic Impurities Concentration System (ICS).
  June
  Common tests of the system. (Cryogenic, vacuum, slow control).
  Suppression of the mechanical resonances at cryogenic temperatures.
  Optimization of the TPC resolution based on signals from the α-source.
  Calibration of the temperature sensors in CryoTPC.
  Connecting of CryoTPC to circulation system (CHUPS) and ICS purification.
  Test of the ICS and impurity detection at the 1 ppb level.

- **DAQ and electronics.** The MuSun DAQ must provide stable data taking over a prolonged period of time, handle a high (15 MB/s) data rate and must not introduce any significant deadtimes. In order to store the incoming high data rate, we will upgrade

our tape system to either a new LTO5 tape robot or alternatively migrate to a disk based storage system.

It is also our goal to upgrade some of the older electronics systems with modern FPGA based logic units in order to improve the overall stability of the detector and data acquisition electronics.

6.2 Beam Time Request

Our beamtime request for 2011 is a follows:

12 weeks of beam time including 2 weeks setup from June 20 to September 12, 2011 in the area πE3. It is mandatory that the same standard MuSun beamline including vertical separator and MuLan kicker is installed.

6.3 Future Plans and Request for enlarged πE1 area

The last request addresses our concern regarding the phasing out of nuclear/particle physics experiments in the πE3 area by 2012. Though the collaboration expects to reach in 2011 a significant first result of the μd capture rate, the experiment needs more time to explore its full physics potential. As outlined in the proposal the pure production beam time is estimated to be 22 weeks of which we can hope to have consumed about one third by the end of 2011.

Our future plans are therefore to continue the MuSun experiment beyond 2011 at the πE1 beamline which was offered by the PSI management as an alternative to the πE3 beam. A one-week feasibilty test was undertaken by a LTP group in August 2010 and has demonstrated that πE1 can deliver low energy muon beams of comparable quality and intensity as πE3 [22]. At the relevant condition (40 MeV/c, momentum bite 4%) a flux of $2{\cdot}10^5 \mu^- s^{-1}$ was observed.

However, to setup at the πE1 port a new muon beamline with kicker, separator and sufficient experimental space, it is necessary to enlarge the πE1 area space toward the low energy area NE-B which is presently no more in use. A study of such an enlargement by the PSI secundary beam group is underway.

We request that PSI enlarges during the year 2012 the πE1 area space toward the low energy area NE-B, such that it will suit future low energy muon experiments in particle physics.

For the MuSun collaboration, moving to the πE1 area means a greater effort of experimental rearrangements and beam studies before μd capture data taking can be resumed. We hope to begin this effort in fall 2012.

References

[1] MuSun Collaboration (http://muon.npl.washington.edu/exp/MuSun): V.A. Andreev, R.M. Carey, V.A. Ganzha, A. Gardestig, T. Gorringe, F.E. Gray, D.W. Hertzog, M. Hildebrandt, L. Ibanez, P. Kammel, B. Kiburg, S.A. Kizilgul, S. Knaack, P.A. Kravtsov, A.G. Krivshich, K. Kubodera, B. Lauss, M. Levchenko, K.R. Lynch, E.M. Maev, O.E. Maev, F. Mulhauser, M. Murray, F. Myhrer, C. Petitjean, G.E. Petrov, J. Phillips, R. Prieels, N. Raha, G.N. Schapkin, N. Schroeder, G.G. Semenchuk, M.A. Soroka, V. Tishchenko, A.A. Vasilyev, A.A. Vorobyov, N. Voropaev, M.E. Vznuzdaev, P. Winter.

[2] Kammel, P. and Kubodera, K. *Annu. Rev. Nucl. Part. Sci.* **60**, 32753 (2010).

[3] Andreev, V. A. et al. *Phys. Rev. Lett.* **99**, 032002 (2007).

[4] Weinberg, S. Phys. Lett. B, **251**, 288 (1990); Nucl. Phys. B, **363**, 3 (1991); Phys. Lett. B, **295**, 114 (1992).

[5] Ando, S., Park, T. S., Kubodera, K., and Myhrer, F. *Phys. Lett.* **B533**, 25–36 (2002).

[6] Chen, J.-W., Inoue, T., Ji, X.-d., and Li, Y.-c. *Phys. Rev.* **C72**, 061001 (2005).

[7] Ricci, P. and Truhlik, E. *arXiv:1012.2216* (2010).

[8] Ricci, P., Truhlik, E., Mosconi, B., and Smejkal, J. *Nucl. Phys.* **A837**, 110–144 (2010).

[9] Marcucci, L. E. et al. *submitted to Phys. Rev. C* (2010).

[10] K. Kubodera and F. Myhrer; E. Epelbaum and Ulf-G. Meissner, private communication.

[11] Tatara, N., Kohyama, Y., and Kubodera, K. *Phys. Rev.* **C42**, 1694–1717 (1990).

[12] Adam, J., Truhlik, E., Ciechanowicz, S., and Schmitt, K. M. *Nucl. Phys.* **A507**, 675–697 (1990).

[13] Chen, J.-W., Ji, X.-d., and Li, Y.-c. *Phys. Lett.* **B620**, 33–41 (2005).

[14] Bardin, G. et al. *Nucl. Phys.* **A453**, 591 (1986).

[15] Cargnelli, M. et al. In *Proceedings of the XXIII Yamada Conf. on Nuclear Weak Processes and Nuclear Structure, Osaka, Japan*, (1989).

[16] Aharmim, B. et al. *Phys. Rev. Lett.* **101**, 111301 (2008).

[17] Butler, M., Chen, J.-W., and Vogel, P. *Phys. Lett.* **B549**, 26–31 (2002).

[18] Chen, J.-W., Heeger, K. M., and Robertson, R. G. H. *Phys. Rev.* **C67**, 025801 (2003).

[19] Park, T. S. et al. *Phys. Rev.* **C67**, 055206 (2003).

[20] Butler, M., Chen, J.-W., and Kong, X. *Phys. Rev.* **C63**, 035501 (2001).

[21] Ganzha, V. A. et al. *Nucl. Instrum. Meth.* **A578**, 485–497 (2007).

[22] Papa, A., Ries, D., Antognini, A., and Petitjean, C. *ETH Semesterarbeit (unpublished)* , 1–17 (2011).